metals

IMPACT FACTOR 2.9

CITESCORE 4.4

Article

# Enhancing Mechanical and Biocorrosion Response of a MgZnCa Bulk Metallic Glass through Variation in Spark Plasma Sintering Time

Bin Shi Jie Bryan, Kai Soon Fong, Chua Beng Wah, Sravya Tekumalla, Min Kyung Kwak, Eun Soo Park and Manoj Gupta

Special Issue

Feature Papers in Biobased and Biodegradable Metals

Edited by

Prof. Dr. Xiaobo Zhang

MDPI

https://doi.org/10.3390/met13081487

*metals*

MDPI

*Article*

# Enhancing Mechanical and Biocorrosion Response of a MgZnCa Bulk Metallic Glass through Variation in Spark Plasma Sintering Time

**Bin Shi Jie Bryan [1], Kai Soon Fong [2], Chua Beng Wah [2], Sravya Tekumalla [3], Min Kyung Kwak [4], Eun Soo Park [4] and Manoj Gupta [1,*]**

[1] Department of Mechanical Engineering, National University of Singapore, Singapore 117576, Singapore
[2] Singapore Institute of Manufacturing Technology (SIMTech), Agency for Science, Technology and Research (A*STAR), 5 CleanTech Loop #01-01, CleanTech Two Block B, Singapore 636732, Singapore
[3] Department of Mechanical Engineering, University of Victoria, 3800 Finnerty Road, Victoria, BC V8W 2Y2, Canada
[4] Department of Materials Science and Engineering, Research Institute of Advanced Materials & Institute of Engineering Research, Seoul National University, Seoul 08826, Republic of Korea
* Correspondence: mpegm@nus.edu.sg

**Abstract:** Development of metallic glasses is hindered by the difficulties in manufacturing bulk parts large enough for practical applications. Spark plasma sintering (SPS) has emerged as an effective consolidation technique in the formation of bulk metallic glasses (BMGs) from melt-spun ribbons. In this study, $Mg_{65}Zn_{30}Ca_5$ melt-spun ribbons were sintered at prolonged sintering times (15 min to 180 min) via SPS under a pressure of 90 MPa and at a temperature of 150 °C (which is below the crystallization temperature), to provide an insight into the influence of sintering time on the consolidation, structural, and biodegradation behavior of Mg-BMGs. Scanning Electron Microscopy was used to characterize the microstructure of the surface, while the presence of the amorphous phase was characterized using X-ray diffraction and Electron Backscatter Diffraction. Pellets 10 mm in diameter and height with near-net amorphous structure were synthesized at 150 °C with a sintering time of 90 min, resulting in densification as high as 98.2% with minimal crystallization. Sintering at extended durations above 90 min achieved higher densification and resulted in a significant amount of local and partial devitrification. Mechanical properties were characterized via compression and microhardness testing. Compression results show that increased sintering time led to better structural integrity and mechanical properties. Notably, SPS150_90 displayed ultimate compressive strength (220 MPa) that matches that of the cortical bone (205 MPa). Corrosion properties were characterized via potentiodynamic polarization with Phosphate Buffered Solution (PBS). The results suggest that the sintered samples have significantly better corrosion resistance compared to the crystalline form. Overall, SPS150_90 was observed to have a good balance between corrosion properties (10× better corrosion resistance to as-cast alloy) and mechanical properties.

**Keywords:** magnesium-based bulk metallic glass; spark plasma sintering; melt spinning; mechanical properties; biocorrosion properties

check for updates

**Citation:** Bryan, B.S.J.; Fong, K.S.; Wah, C.B.; Tekumalla, S.; Kwak, M.K.; Park, E.S.; Gupta, M. Enhancing Mechanical and Biocorrosion Response of a MgZnCa Bulk Metallic Glass through Variation in Spark Plasma Sintering Time. *Metals* **2023**, *13*, 1487. https://doi.org/10.3390/met13081487

Academic Editors: Golden Kumar and Jiro Kitagawa

Received: 24 July 2023
Revised: 8 August 2023
Accepted: 16 August 2023
Published: 18 August 2023

**Copyright:** © 2023 by the authors. Licensee MDPI, Basel, Switzerland. This article is an open access article distributed under the terms and conditions of the Creative Commons Attribution (CC BY) license (https://creativecommons.org/licenses/by/4.0/).

## 1. Introduction

Magnesium-based metallic glasses have been studied extensively in recent years for a wide range of biomedical applications [1,2]. These metallic glasses are different from traditional metallic alloys as they exist in the amorphous state and are shown to exhibit excellent corrosion resistance and yield strength [1,3]. Coupled with their good biocompatibility in vivo [4], magnesium-based bulk metallic glasses have great potential in the biomedical sector as an alternative class of absorbable implant biomaterials [5].

Despite the numerous advantages of bulk metallic glasses, very few have made it to the manufacturing stage. This is because the synthesis of bulk metallic glasses

(BMGs) is extremely challenging, owing to the need for extremely high cooling rates of ~$10^4$–$10^5$ °C/s [6]. Different densification methods have been proposed to obtain BMGs, including warm extrusion [7,8], equal channel angular extrusion [9], selective laser sintering [10], and spark plasma sintering [11]. Among them, spark plasma sintering (SPS) has garnered special interest as a post-consolidation method due to its high throughput power consolidation, which is assisted by elevated temperature and pressure [12].

Sintering is a process in which materials are compacted into solid-state objects. The bonding of sintered particles via atomic diffusion mechanics is governed by both heat and pressure [13]. Since Mg-based BMGs have a relatively low working temperature range of up to 150 °C in Mg-Zn-Ca metallic glass, SPS has shown to be extremely useful in the synthesis of Mg-based BMGs owing to its precise temperature control and high pressure [11]. Any temperature above 150 °C would result in the nucleation of crystals, destroying the amorphous nature of the BMG [11].

In our previous paper, we devised a two-step synthesis process involving melt spinning and spark plasma sintering to successfully fabricate fully amorphous Mg-based bulk metallic glass pellets with a diameter of 10 mm and high corrosion resistance [11]. However, their structural integrity and mechanical properties were not ideal because of the presence of significant porosity and the lack of inter-atomic bonding during the SPS process.

Accordingly, this research focuses on refining the SPS process through three objectives: (i) improving the structural integrity and mechanical properties of Mg-Zn-Ca BMG, while maintaining a complete amorphous nature by increasing sintering time; (ii) understanding the effect of sintering time on diffusion mechanics; and (iii) maintaining good biocorrosion resistance post SPS.

## 2. Materials and Methods

### *2.1. Materials*

An alloy ingot with a composition of $Mg_{65}Zn_{30}Ca_5$ (as-cast) was synthesized via Disintegrated Melt Deposition (DMD), and the raw materials used are detailed in Table 1 below. The raw materials were melted at a target superheat temperature of 750 °C, followed by stirring of the melt at 420 rpm for 5 min before casting.

**Table 1.** Raw materials used in the synthesis of $Mg_{65}Zn_{30}Ca_5$.

| Raw Material | Supplier |
|---|---|
| Magnesium (Mg) turnings, 99.9% purity | ACROS Organics, Waltham, MA, USA |
| Zinc (Zn) granules, 99.8% purity | Alfa Aesar, Waltham, MA, USA |
| Calcium (Ca) granules, 99.8% purity | Alfa Aesar, Waltham, MA, USA |

### *2.2. Synthesis*

The master alloy (5 g) was melt-spun in a quartz crucible under an argon atmosphere with a copper spinning wheel turning at 2000 rpm, with the argon injection pressure set at 450 mbar. The distance between the nozzle of the quartz crucible and the copper wheel was controlled at 0.5 mm. Amorphous ribbons of the alloy were produced with a thickness and width of ~0.1 mm and 3 mm, respectively. A schematic of the melt spinning setup is shown in Figure 1.

The amorphous ribbons obtained were mechanically milled into powder and compressed at room temperature using a 10 mm compaction die in a hydraulic press under 500 psi pressure for 1 min.

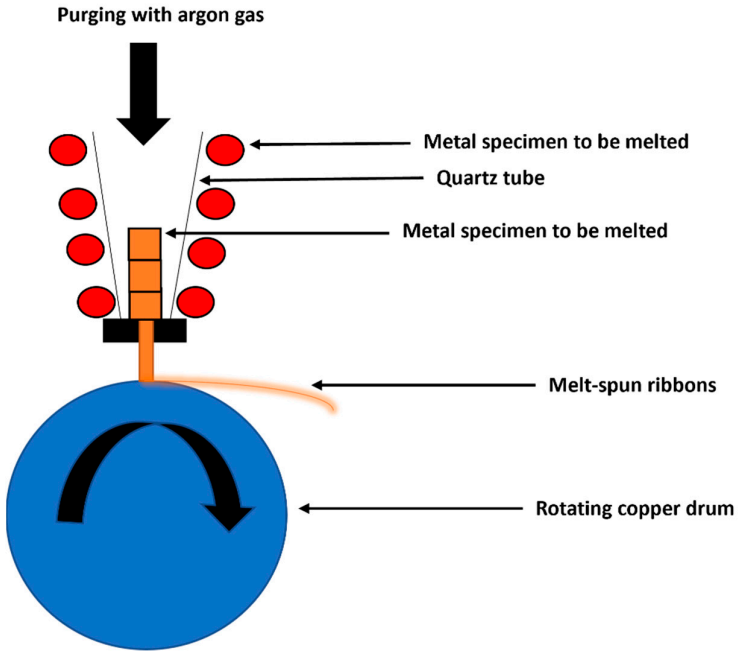


**Figure 1.** Schematic illustration of the melt spinning process.

Finally, the compacted powder was sintered into pellets, with a diameter of 10 mm and a height of 10 mm, via SPS. A DR. SINTER LAB Jr. SERIES 632LX machine from Fuji Electronics was utilized for this process, operating under vacuum conditions (<3 Pa) and featuring a maximum sintering DC pulse of 3000 A. A K-type thermocouple was employed to monitor and regulate the temperature. During the sintering process, the ribbons were placed in a high-strength carbon die at a pressure of 90 MPa and at 150 °C. The temperature of 150 °C was established as the optimal operating temperature, beyond which crystallization occurs [11]. A schematic illustration of the SPS technique is shown in Figure 2.

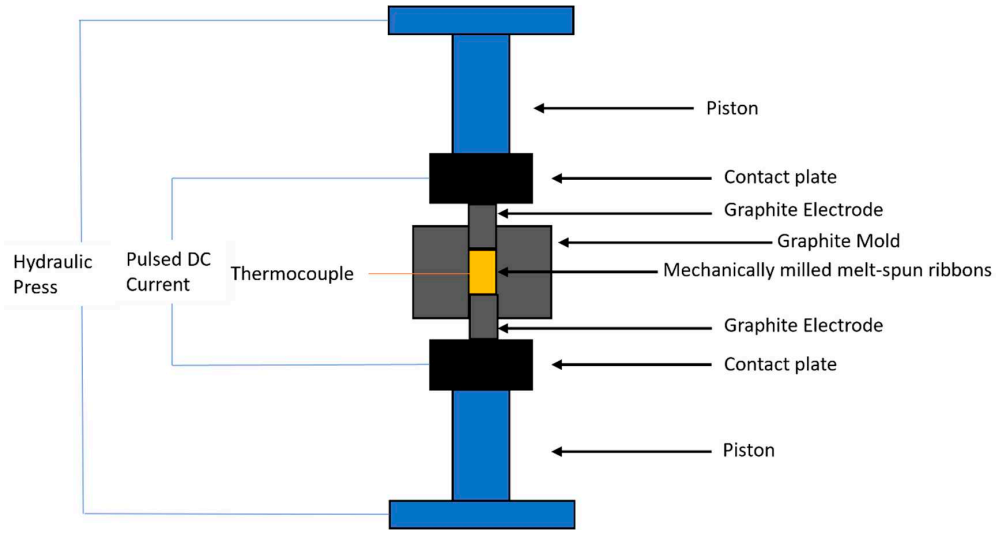


**Figure 2.** Schematic illustration of spark plasma sintering.

The initial heating rate was held at 15 K/min but was gradually reduced to 7 K/min near the end of the heating process to avoid overheating. Table 2 presents the specific processing parameters for each sample, with designations such as SPS150_15 representing a sample sintered at 150 °C for 15 min.

**Table 2.** Spark plasma sintering operating parameters and experimental procedure.

| | Starting Temp (°C) | Heating Rate (°C/min) | Time (min) | Heating Rate (°C/min) | Time (min) | Final Temperature (°C) | Sintering Time (min) | Force (kN) | Pressure (MPa) |
|---|---|---|---|---|---|---|---|---|---|
| SPS150_15 | 30 | 15 | 4 | 7 | 8.6 | 150 | 15 | 7 | 90 |
| SPS150_30 | 30 | 15 | 4 | 7 | 8.6 | 150 | 30 | 7 | 90 |
| SPS150_60 | 30 | 15 | 4 | 7 | 8.6 | 150 | 60 | 7 | 90 |
| SPS150_90 | 30 | 15 | 4 | 7 | 8.6 | 150 | 90 | 7 | 90 |
| SPS150_180 | 30 | 15 | 4 | 7 | 8.6 | 150 | 180 | 7 | 90 |

### *2.3. Characterization*

#### 2.3.1. Surface Morphology

The spark plasma-sintered samples were ground with 1200 grit SiC paper for XRD analysis and polished up to a 0.05 µm finish using a diamond suspension for SEM/EBSD studies. During each polishing step, the samples were cleaned ultrasonically for 5 min with ethanol. The microstructure of the spark plasma-sintered samples was analyzed using both an OLYMPUS metallographic optical microscope and a JEOL JSM-6010 Scanning Electron Microscope (SEM). The spark plasma-sintered samples were also analyzed using a Shimadzu LAB-XRD 6000 X-ray diffractometer for phase identification. The diffractometer had a Cu $K_\alpha$ radiation source ($\lambda$ = 0.1541 nm), and a scan speed of 2°/min was used for phase identification. To confirm the amorphous nature of the samples, electron backscattered diffraction (EBSD) was performed using a Gemini SEM 450 (Carl Zeiss Microscope GmbH, Germany) high-resolution scanning electron microscope equipped with an EDAX EBSD system with a velocity camera. Prior to EBSD, the samples were polished using a water-free oxide polishing suspension and were cleaned using lab grade ethanol. Additionally, the samples also underwent ion polishing for 2 h using the PECS II system by Gatan to remove any residual surface deformation/oxide layers.

#### 2.3.2. Density and Porosity

Density measurements were conducted following Archimedes' principle. The samples were initially weighed in air and then in distilled water using an A&D ER-182A electronic balance (Bradford, Massachusetts) with an accuracy of ±0.0001 g. Table 3 below shows the composition and density of the alloy synthesized in this work.

The experimental density of the alloy was determined via Equation (1) below:

$$p_E = \frac{w_{air} \times p_{water} - w_{water} \times p_{air}}{w_{air} - w_{water}} \quad (1)$$

where $p_E$ represents the experimental density of the alloy in g/cm$^3$, w is the weight of specimen, and $p_{air}$ and $p_{water}$ refer to the density of air and water, respectively, in g/cm$^3$.

The difference between experimental densities of the as-cast alloy compared to the experimental density of the sintered samples can be used to calculate the porosity levels within the sintered sample, as governed by Equation (2) below:

$$\text{Porosity}(\%) = \frac{p_1 - p_2}{p_2} \times 100 \quad (2)$$

where $p_1$ and $p_2$ represent the experimental density of the as-cast master alloy and sintered samples, respectively, in g/cm$^3$.

**Table 3.** Composition and densities of the $Mg_{65}Zn_{30}Ca_5$ synthesized in this work.

| Material Composition | Raw Materials Composition by Weight % | Theoretical Density ($g/cm^3$) | Actual Density ($g/cm^3$) |
|---|---|---|---|
| $Mg_{65}Zn_{30}Ca_5$ | Mg 42.2%<br>Zn 52.42%<br>Ca 5.36% | 2.86 | 2.85 |

#### 2.3.3. Mechanical Properties

Vickers hardness measurements were made using a Shimadzu-HMW automatic digital microhardness tester. A load of 245.2 mN and a 15s dwell time were utilized for each indentation across the sample surface. This set of parameters is in line with ASTM standard E384-08. At least 20 indentations were obtained for each sample.

Following this, compression testing was conducted using an MTS 810 fully automated servo hydraulic mechanical testing machine. The strain rate was set at $8.33 \times 10^{-5}$ $s^{-1}$, with height and diameter set to 10 mm (height-to-diameter ratio of 1).

#### 2.3.4. Biocorrosion Tests

The biocorrosion tests were performed via an electrochemical cell setup. The spark plasma-sintered sample was used as the working electrode, the counter electrode was a graphite rod, and a Saturated Calomel Electrode (SCE) was used as the reference electrode. Lastly, the electrolyte used in this study was Phosphate Buffered Solution (PBS) from Life Technologies, Singapore, with a pH of 7.4.

The system was left as an open circuit for 60 min before being polarized at a voltage of −200 mV vs. their open circuit potential (OCP) to +200 mV vs. their OCP, with a scan rate of 1 mV $s^{-1}$. To simulate body conditions, the electrolyte was maintained at 37 °C via a water bath. A Gamry Reference 600 potentiostat was used for data collection, while a Solatron Analytical SI 1287 was used for data analysis.

## 3. Results

### *3.1. Spark Plasma Sintering of Mg-Zn-Ca BMGs*

There are a few parameters that can be optimized with SPS, namely pressure, sintering temperature, and sintering time. In the present study, pressure was kept constant at 90 MPa, which is the maximum pressure that can be safely exerted on the high-strength carbon die. Sintering temperature was maintained at 150 °C, which is the optimal working temperature of $Mg_{65}Zn_{30}Ca_{5,}$ above which crystallization occurs that destroys the amorphous nature [11]. Therefore, this study focused on the effect of elevated sintering time on the amorphous nature, mechanical properties, and biocorrosion properties of MgZnCa BMGs.

The BMGs were successfully sintered by SPS at 150 °C with a sintering time of up to 180 min. The effect of sintering time on the amorphous characteristics of MgZnCa BMGs can be observed by the XRD patterns in Figure 3. The amorphous nature of the BMG was largely maintained for up to 90 min of sintering time, as shown by the diffused broad peak at ~2θ = 38°. The XRD results also show very minute peaks across the diffused region at ~2θ = 37° in all sintered samples. Here, diffraction peaks superimposed onto the amorphous halo for all sintered samples could be observed, indicating that some form of crystallinity exists and that the sintered samples are predominantly but not completely amorphous. At an extended sintering time of above 90 min, significant crystalline peaks start to emerge such as that in SPS150_180. These peaks correspond to crystalline Mg-Zn and α-Mg phases which indicate that crystallization has occurred, disrupting the homogenous amorphous matrix.

To account and check for the amorphous nature of the samples post sintering, a differential scanning calorimeter was utilized. Here, selected DSC scans of SPS150_90 and SPS150_180 are shown in Figure 4a,b. The two samples were used for comparison because there was a sharp change in the XRD patterns from SPS150_90 to SPS150_180,

as shown in Figure 3. Contrast in the DSC trace could be observed. SPS150_90 showed an onset of glass transition ($T_g$) and subsequent crystallizations, with the first onset of crystallization denoted as $T_x$ at ~160–170 °C in Figure 4b. This glass transition and the first crystallization temperatures are in line with studies reported on similar Mg-Zn-Ca metallic glass systems [14–16]. On the other hand, SPS150_180 is lacking the onset of glass transition and crystallization, as shown in Figure 4b. Therefore, the DSC scans prove that SPS150_90 is predominantly in the amorphous state with a very small amount of crystallinity, while SPS150_180 recrystallized to a certain degree.

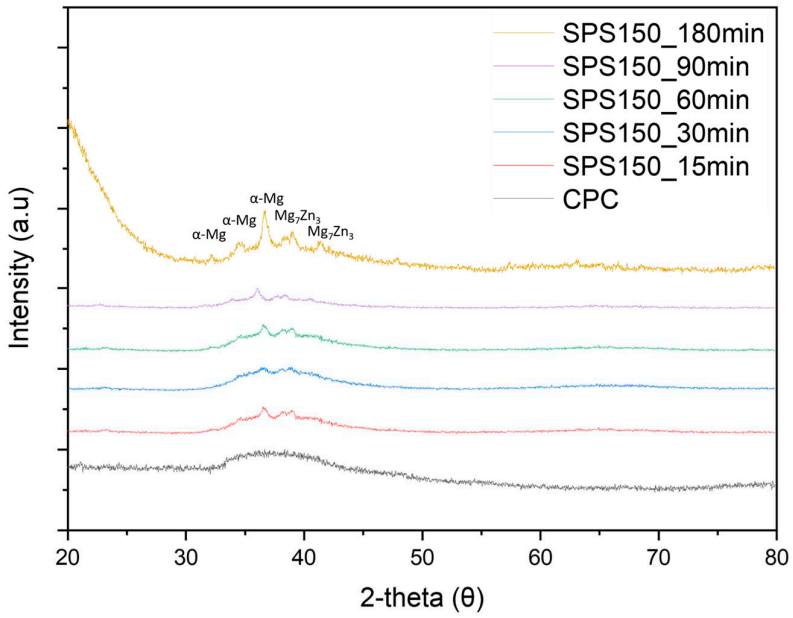


**Figure 3.** XRD patterns of pre-SPS cold compacted (CPC) and spark plasma-sintered Mg-Zn-Ca ribbons at varying sintering times from 15 to 180 min.

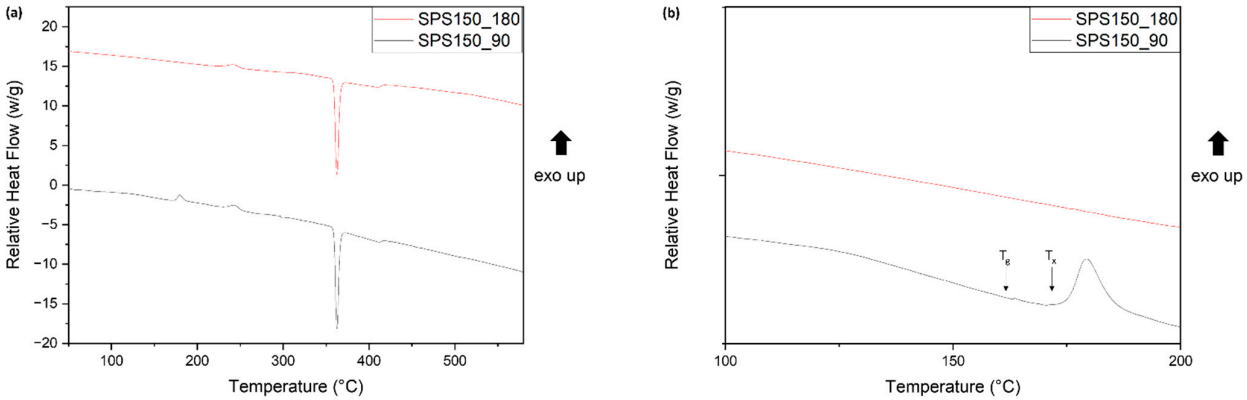


**Figure 4.** Comparison of DSC traces between SPS150_90 and SPS150_180 (**a**) across the full range of temperatures (50 °C to 600 °C) and (**b**) a magnified view of 100 °C to 200 °C.

EBSD was also performed to analyze microstructural features in SPS150_180 to confirm the presence of grains, which showed the presence of crystallinity. From the EBSD Inverse Pole Figure (IPF) map in Figure 5a, grains can clearly be indexed in SPS150_180; α-Mg crystalline phase was identified with a final grain size of 2.70 ± 1.9 μm and a significant amount of crystallinity, as shown in Figure 5b. On the other hand, no grains could be indexed with SPS150_90, which suggests that the presence of crystallinity, while present, is minimal. These results are consistent with our data collected from XRD, suggesting that significant dynamic crystallization occurred with prolonged sintering times above 90 min.

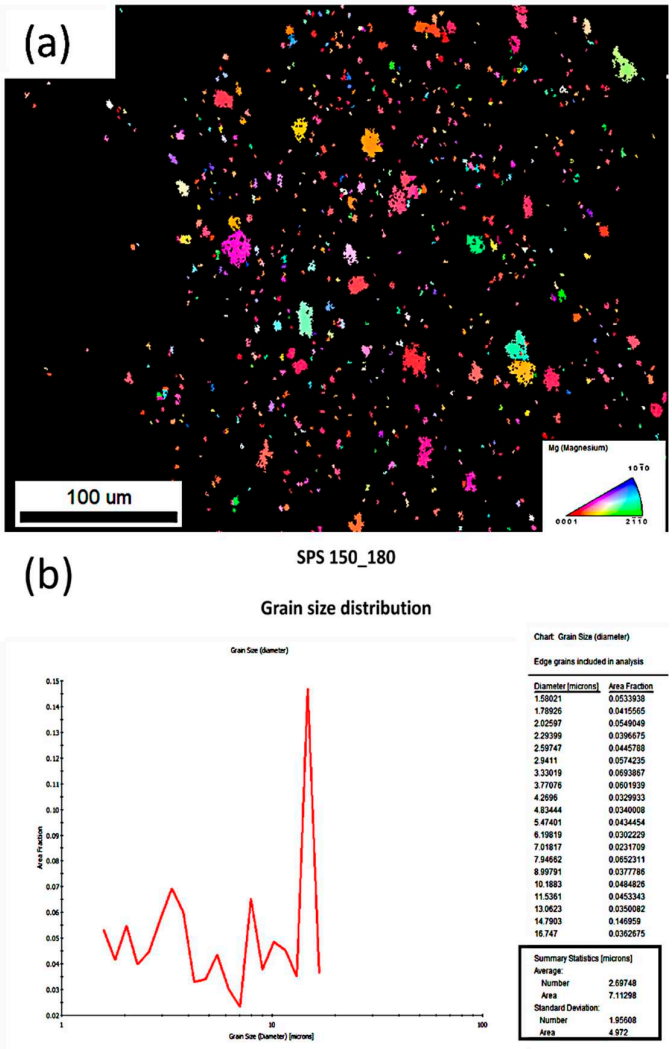


**Figure 5.** Electron backscattered diffraction patterns of MgZnCa: (**a**) IQ + IPF map and (**b**) grain size distribution.

The surface morphologies of the pre-SPS powder and the spark plasma-sintered BMGs at different sintering times (15 to 180 min) compared to the as-cast alloy are shown in Figure 6. Here, we can look at the effect of sintering time on surface morphology. At lower sintering times (15–30 min), it can be observed that the powders are not bonded together, as shown by the large gaps between the powders in Figure 6b,c. In addition, the contrasting layers seen in Figure 6b,c show that any form of bonding between layers is lacking, with the presence of a significant amount of porosity on the surface also shown.

At higher sintering times (60–180 min), the interparticle distances are significantly reduced and there is minimal porosity present, as shown in Figure 6d–f. Unlike the flaky appearance due to the presence of contrasting layers seen at lower sintering times, a smooth and homogenous texture was observed at higher sintering times. Denoted by the circles in Figure 6d–f, these are areas in which the interfaces among powder particles start to fade away, forming a more homogeneous matrix. These could suggest that, at elevated sintering times, short-order diffusion of atoms may have occurred between adjacent powder particles, resulting in some form of chemical and mechanical interlocking which is likely to promote better structural integrity.

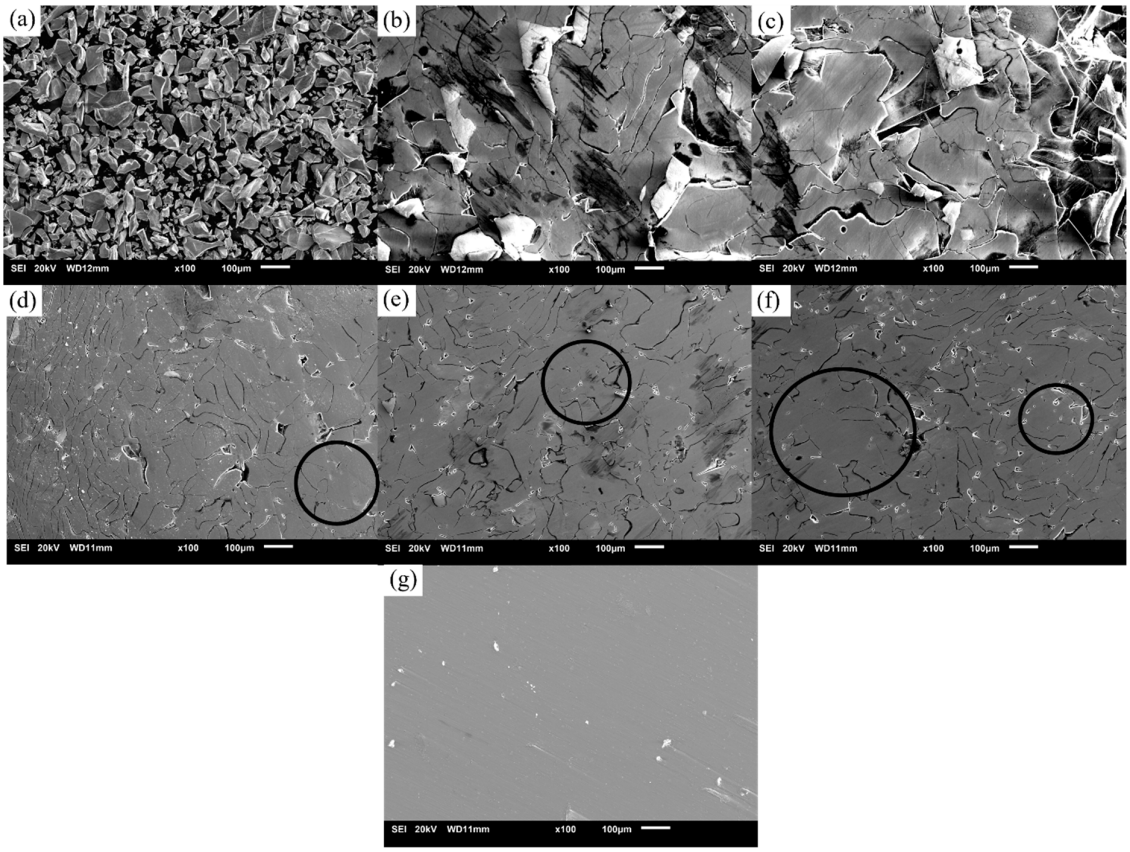


**Figure 6.** SEM micrographs of (**a**) pre-sintered Mg-Zn-Ca powder, spark plasma-sintered Mg-Zn-Ca BMGs with (**b**) 15 min, (**c**) 30 min, (**d**) 60 min, (**e**) 90 min, and (**f**) 180 min sintering times, and (**g**) as-cast alloy. Here, the dark circles show regions in which the interfaces between ribbons could have been diffused.

Comparing Figure 6d–f, we can observe that the further increase in sintering time from 60 min to 180 min had minimal impact on porosity (1.88 vol. % in SPS150_60 to 1.22 vol. % in SPS150_180). This may be attributed to a lack of long-range diffusion in atoms that typically require higher temperature [17].

### *3.2. Density and Porosity*

The measured densities and derived porosities of Mg-Zn-Ca spark plasma-sintered BMGs compared to as-cast Mg-Zn-Ca alloy are shown in Figure 7. The densities of SPS150_15, SPS150_30, SPS150_60, SPS150_90, and SPS150_180 are 2.74 g/cm$^3$, 2.76 g/cm$^3$, 2.81 g/cm$^3$, 2.82 g/cm$^3$, and 2.83 g/cm$^3$, respectively, while their respective porosities are 4.29%, 3.70%, 1.88%, 1.53%, and 1.22%. The porosity values are derived by comparing density values to the density of the as-cast Mg-Zn-Ca alloy. Here, increased sintering time has shown to be successful in reducing porosity by ~70% while maintaining the amorphous nature of the BMGs. With an extended sintering time above 60 min, the porosities of spark plasma-sintered samples remained low and represent those of near-net-shaped products (~2%).

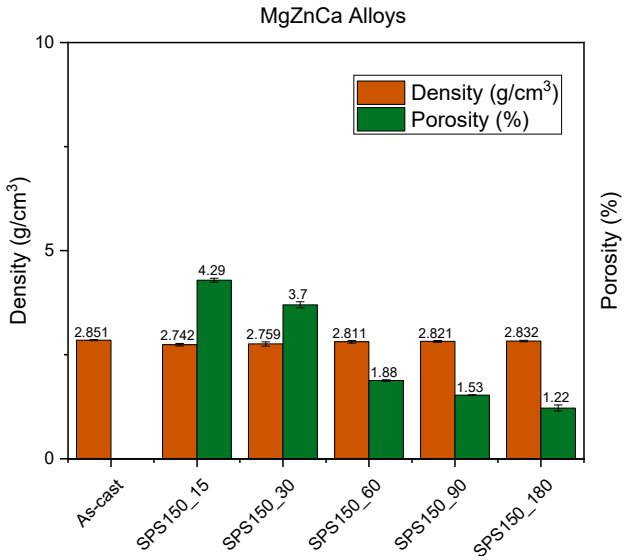


**Figure 7.** Density and porosity of Mg-Zn-Ca BMGs at different sintering times.

### *3.3. Mechanical Properties*

Figure 8 shows the Vickers hardness results of spark plasma-sintered BMGs under different sintering times. The results have shown that the hardness value increases with increasing sintering time, with a maximum value of ~430 HV exhibited by SPS150_180. Generally, Vickers hardness highly depends on the volume fraction of pores [18]. From SPS150 to SPS150_180, the porosity reduced significantly, as discussed earlier (4.29% compared to 1.22%). Therefore, we can observe that the hardness of the material increased from ~350 HV to ~430 HV. While there was a slight reduction in hardness from ~361 HV in SPS150_15 to ~353 HV in SPS150_30, the difference is insignificant in the overall trend.

However, the hardness of the material did not change significantly from SPS150_90 to SPS150_180 despite doubling the sintering time and further reducing porosity (1.53% to 1.22%). This could be due to the presence of grains that could allow for easier dislocation motion in amorphous matrices within SPS150_180, resulting in a drop in hardness.

The as-cast sample is expected to have a significantly lower hardness of 75 HV as it is in a complete crystalline state. This hardness value for the as-cast alloy is in line with other studies conducted on crystalline Mg-based alloys [18–20].

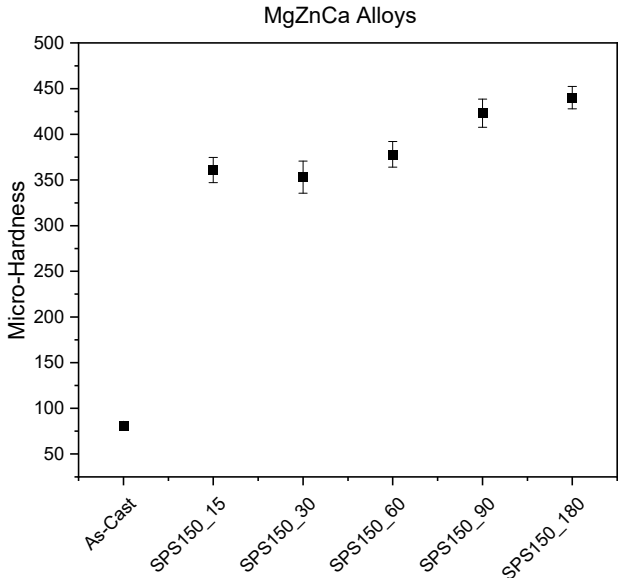


**Figure 8.** Microhardness of Mg-Zn-Ca BMGs at different sintering times.

The mechanical properties of sintered samples were also investigated by compression tests. Engineering stress–strain curves of all samples are shown in Figure 9. Calculated values of ultimate compression strength (UCS), fracture strain, and energy absorbed are shown in Table 4. The results show a notable improvement in UCS and fracture strain with increasing sintering time. The increase in sintering time from 15 min to 180 min resulted in an increase in UCS from 108 MPa to 254 MPa.

Comparing both the hardness and compressive strength of the materials, we can observe a discrepancy in the results: the hardness value of the as-cast alloy is the lowest, while compressive strength is the highest. This could be because the hardness measurement was more of a surface indentation, which is relatively independent of the bulk sample and does not provide a full representation of the structural integrity of the bulk sample. The nature of the sintering process (which is significantly below the melting temperature of the alloy) would mean that voids within the sintered samples are present. Additionally, the lack of melting would mean that the interlocking between particles would not be as strong (think of two particles being melting together compared to two particles compacted together). This phenomenon would not be captured by the surface indenter but would be captured by the compression tests as it involves the entire bulk sample.

**Table 4.** Compressive response of Mg-Zn-Ca BMGs sintered for various lengths of time.

| Sample Name | UCS (MPa) | Reference |
|---|---|---|
| As-cast | 324 ± 10 | - |
| Cortical bone | 205 ± 17 | [21] |
| SPS150_15 | 108 ± 10.5 | - |
| SPS150_30 | 143 ± 7.4 | - |
| SPS150_60 | 187 ± 8.9 | - |
| SPS150_90 | 220 ± 5.3 | - |
| SPS150_180 | 254 ± 7.2 | - |

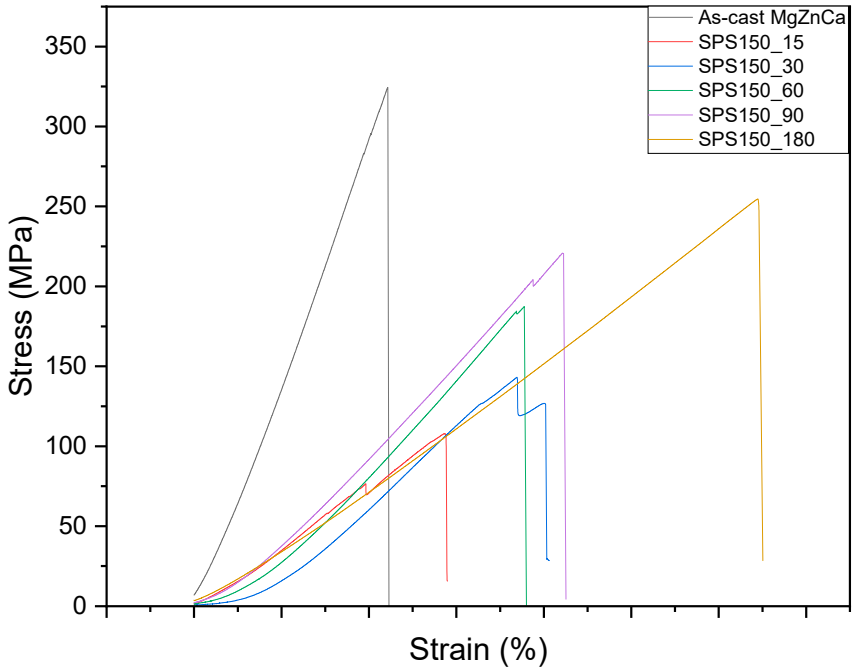


**Figure 9.** Compressive stress–strain curves of Mg-Zn-Ca BMGs with various sintering times.

In our earlier discussion, the SEM images of the sintered samples, particularly those with more than 60 min of sintering time, had ribbon interfaces that started fading away,

forming a more homogenous matrix. This, coupled with a reduction in porosity, could possibly explain why we see a significant improvement in UCS with prolonged sintering time. The mechanical properties of the sintered samples, particularly SPS150_90, exhibited compressive strength that is similar to cortical bone (220 MPa and 205 MPa, respectively). The similarity in compressive strength can reduce the effect of stress shielding [22], which commonly occurs due to a difference in mechanical properties between the bone and the implant material [23]. Expectedly, SPS150_180 has better mechanical properties among all sintered samples due to its significantly longer sintering time compared to the other samples. However, the presence of crystallization, as shown in Figure 3, will have a detrimental effect on its corrosion resistance, which will be discussed in the next section. Therefore, a careful optimization between mechanical properties and corrosion resistance can be tailored for different applications.

### *3.4. Biocorrosion Properties*

The changes in open circuit potential (OCP) as a function of time after 1 h of immersion in Phosphate Buffer Solution (PBS) at 37 °C are shown in Figure 10. Here, OCP refers to the potential difference between the working electrode (metal surface to be studied) and the reference electrode [24]. The $E_{ocp}$ values for as-cast crystalline MgZnCa and SPS150_15, SPS150_30, SPS150_60, SPS150_90, and SPS150_180 MgZnCa BMGs are −1.47 V, −1.32 V, −1.27 V, −1.25 V, −1.35 V, and −1.4 V, respectively. The less negative the corrosion potential, the lower the tendency for corrosion in PBS [25]. Minor changes in $E_{ocp}$ were noticed from SPS150_15 to SPS150_90, with SPS150_60 having the most positive potential among the sintered samples. SPS150_180 and crystalline as-cast MgZnCa, on the other hand, have significantly more negative potential values, signaling a significant reduction in corrosion resistance as compared to the other sintered samples.

From the OCP data, it can be observed that the OCP was fairly smooth and stable from SPS150_15 to SPS150_90. This suggests the formation of a passive film on the surface. SPS150_180 and the crystalline as-cast alloy, on the other hand, showed significant fluctuations in OCP across the entire duration. This would suggest that the passive film formed on the surface is unstable, resulting in the continuous re-passivation and de-passivation of the oxide film [26].

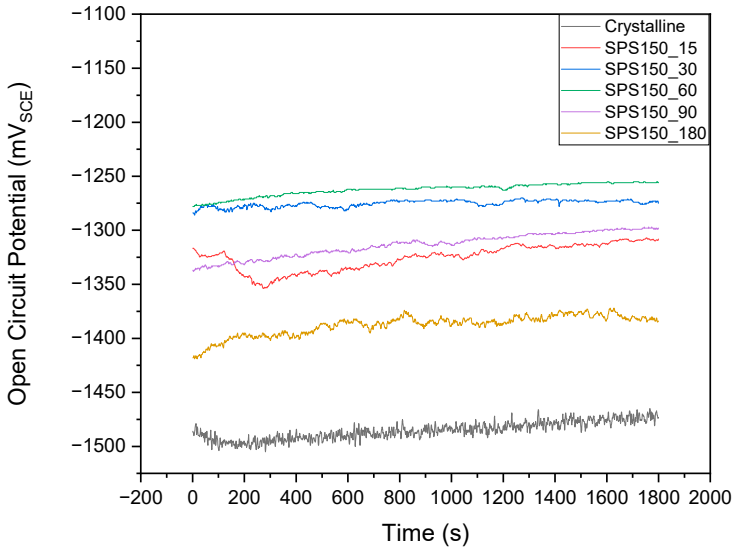


**Figure 10.** Time dependence of open circuit potential (OCP) across different sintering times.

The potentiodynamic polarization (PDP) curves for the spark plasma-sintered samples as compared to the as-cast crystalline MgZnCa are shown in Figure 11. For a more accurate depiction of results, three scans were performed for each sample. The median trace with

the most representative corrosion current ($i_{corr}$) and corrosion potential ($E_{corr}$) was selected and plotted.

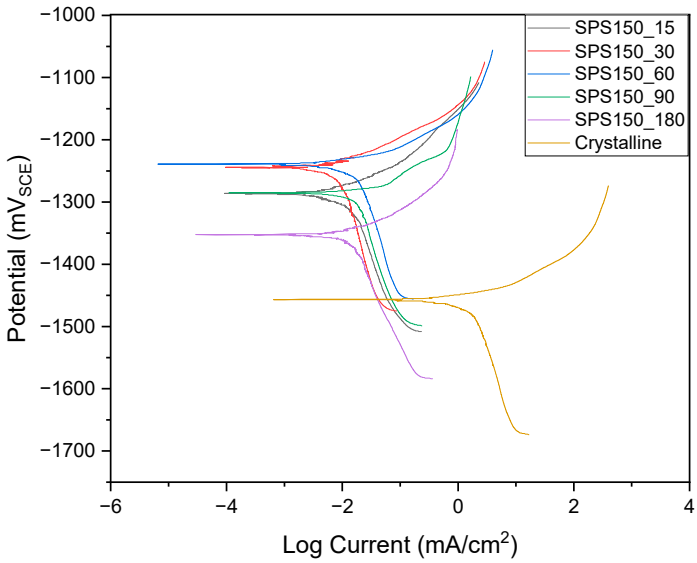


**Figure 11.** Potentiodynamic plot of Mg-Zn-Ca across various sintering times.

From the PDP scans, it was found that the BMGs have more noble corrosion potentials (−1200 to −1350 $mV_{SCE}$) compared to the crystalline MgZnCa (−1470 $mV_{SCE}$), indicating lower corrosion activity. This is likely due to the lack of crystalline phases and because the BMGs are generally free of microstructure defects such as grain boundaries and dislocations, reducing galvanic couples and preventing intergranular and localized pitting corrosion [27]. In addition, the absence of structural defects suppresses ion diffusion, thereby improving corrosion resistance [28].

A closer inspection of the PDP plots reveals that the cathodic reaction kinetics are comparable from SPS150_15 to SPS150_90, indicating similar cathodic activity (hydrogen evolution). When compared to SPS150_180, significantly higher cathodic activity could be observed for the latter. Cathodic activity is extremely important in the application of a biomaterial as the rapid hydrogen evolution can lead to the formation of gas cavities and swelling at the implant site [29].

Comparing the anodic reaction kinetics, the anodic curves showed similar current density values from SPS150_15 to SPS150_90. Corrosion current density is a parameter that closely relates to the degradation resistance of the material. Therefore, a lower corrosion current density would represent better corrosion resistance. However, in SPS150_180, the presence of crystallinity results in a shift to higher current density values and enhanced anodic dissolution.

Table 5 illustrates the Tafel fitting results of the potentiodynamic polarization curves. The corrosion current density ($I_{corr}$) is a parameter that strongly correlates to degradation resistance, while the corrosion rate in mm/year is derived from the following general formula (Equation (3)) [30]:

$$\text{Corrosion Rate in mm/year} = 3.27 \times I_{corr} \times \frac{EW}{p} \quad (3)$$

where $I_{corr}$ represents the corrosion current density ($mA/cm^2$), EW represents the equivalent weight of the material, and $p$ represents the density of the material in $g/cm^3$.

**Table 5.** Corrosion response of Mg-Zn-Ca at various sintering temperatures.

| Sample Name | $I_{corr}$ (mA/cm$^2$) | $E_{corr}$ ($mV_{SCE}$) | Corrosion Rate (mm/Year) |
|---|---|---|---|
| CRYSTALLINE | $19.2 \times 10^{-2}$ | −1469 | 4.086 |
| SPS150_15 | $1.25 \times 10^{-2}$ | −1276 | 0.265 |
| SPS150_30 | $1.01 \times 10^{-2}$ | −1240 | 0.214 |
| SPS150_60 | $1.95 \times 10^{-2}$ | −1200 | 0.413 |
| SPS150_90 | $1.86 \times 10^{-2}$ | −1290 | 0.394 |
| SPS150_180 | $3.91 \times 10^{-2}$ | −1351 | 0.829 |

The corrosion current density and the corrosion rate are directly related, meaning that a higher corrosion current density indicates a higher rate of metal dissolution, which results in a higher corrosion rate [31]. The corrosion rates in Table 5 suggest that corrosion resistance is the most optimal at sintering times of up to 30 min, with a ~20× improvement in corrosion resistance compared to the as-cast crystalline alloy (0.214 mm/year in SPS150_30 compared to 4.086 mm/year in the crystalline MgZnCa alloy).

With prolonged sintering time, however, the corrosion rate increased significantly. The corrosion rate of SPS150_180 was 0.829 mm/year, suggesting a comparable corrosion rate to as-cast crystalline MgZnCa (4.086 mm/year). The results suggest that the presence of a significant amount of crystallinity in SPS150_180, as identified by the EBSD in Figure 5, accelerated the degradation that is otherwise very limited in samples with a 90 min sintering time. It is interesting to note that by increasing sintering time from 30 min to 90 min, the corrosion rate increased ~2× from 0.214 mm/year in SPS150_30 to ~0.413 mm/year in SPS150_90. This increase in corrosion activity may be attributed to the presence of more crystallinity at elevated sintering times.

Nonetheless, all sintered samples in this work showed better corrosion resistance than the crystalline as-cast samples, indicating that a more stable passive film formed on the surfaces. However, the presence of crystalline phases in SPS150_180, as confirmed with the XRD and EBSD studies, had a detrimental effect on corrosion resistance. Therefore, by optimizing sintering time, SPS150_90 has been shown to produce a good balance between mechanical properties and corrosion resistance.

## 4. Discussion

*Influence of Sintering Time on the Densification of Melt-Spun Ribbons*

It is widely known that metallic glasses are prone to structural relaxation and crystallization. Diffusion plays a major role in these processes, and even more so towards the understanding behind the consolidation mechanism during SPS. While the knowledge of diffusion in metallic glasses has been rather limited, temperature-dependent Arrhenius plots on diffusion have been well discussed [32–34]. Often, people have interpreted this as a sign of a diffusion process that resembles that in crystals. In crystals, defects that behave like vacancies at thermal equilibrium are the carriers for diffusion. However, the resulting diffusivity values have sometimes differed greatly from those that are typical of a vacancy mechanism [35].

Spark plasma sintering of BMGs is a relatively new concept. In recent years, some studies have been performed on spark plasma-sintered Zr-based [36] and Fe-based [37] alloys. However, unlike many other materials sintered via SPS, Mg-based BMGs are extremely challenging to obtain. This is due to the temperature constraint during sintering, which is brought forth by the inherently low crystallization temperature of ~160 °C. As such, any sintering temperature used should be below the crystallization temperature of the alloy to prevent the onset of crystallization.

To improve the diffusion rate in amorphous matrices, we can increase the pressure during sintering to force atoms to move through particulate barriers. Increasing pressure can also cause brittle fractures in metallic glass ribbons or particles with little ductility,

resulting in increased surface area and density during sintering. High pressure can overcome limitations set by temperature and has been studied in detail for densification during SPS [38]. The current study was limited to a maximum pressure of 90 MPa due to the constraints imposed by the equipment and compaction die used. However, it is worth noting that industrial grade SPS equipment has been reported to exert much higher pressures of 400–500 MPa. For instance, a paper published by Perriere et al. reported the use of 500 MPa to achieve full densification of amorphous powders [39].

Time dependence on the diffusion kinetics of metallic glasses is less studied. For instance, in a work on diffusion coefficients in metallic glasses by Tyagi et al., it was suggested that enhanced diffusion over the relaxed state of the amorphous solid can be attributed to the diffusion of atoms via excess vacancies, which could be generated due to the mismatch of atomic size during the glass forming process [40]. As a consequence of this enhanced diffusion, which is time- and energy-dependent, an irreversible increase in volume density could be observed [40].

Our results indicate that nearly full densification could be obtained with prolonged sintering time, as shown in the density values in Figure 6. Densification via SPS can be achieved through two steps. Firstly, the initial stages of sintering occur at narrow necks of particle interfaces and would generally result in a localized increase in temperature, where relaxation occurs rapidly due to the high thermal diffusivity of the material. This results in some form of cohesion between particles [11,41]. As the sintering progresses, complete densification could then happen during the second step. This occurs when the necks (regions of contact between neighboring particles) are wide enough, thus allowing for homogeneous heating and Newtonian flow (enhanced diffusion) of the particles within the BMGs, therefore leading to complete densification [37,42].

While our studies have shown that increased sintering time results in better densification, what is notably interesting is that prolonged sintering time can have an effect on the amorphous behavior of the spark plasma-sintered samples. When sintering time was increased from 90 min to 180 min, a significant amount of crystallization was observed by both XRD and EBSD studies, as shown in Figure 3 and Figure 4, respectively. Generally, crystallization requires the nucleation of grains, which is energy-dependent [43]. However, the fact that SPS150_90 shows little signs of crystallization shows that a temperature of 150 °C provides insufficient energy for the nucleation of grains with 90 min of sintering time. While this phenomenon is yet to be studied, a possible explanation could be the enhanced diffusion attributed to prolonged sintering time at elevated pressure (90 MPa) and temperature (150 °C) coupled with the presence of free excess volume in metallic glasses [44].

## 5. Summary

The influence of sintering time on the production of spark plasma-sintered Mg-Zn-Ca BMGs was studied. The experimental results reveal the following:

(1) Increasing the sintering time during the SPS process is effective in improving the density and structural integrity of Mg-Zn-Ca BMGs at 150 °C and 90 MPa.
(2) A predominantly amorphous structure was obtained post SPS with a sintering time of up to 90 min (SPS150_90), with density close to that of the master alloy (2.82 g/cm$^3$ vs. 2.85 g/cm$^3$, ~98.2% densification). Densification increases with increasing sintering time.
(3) SPS150_90 achieved UCS of 220 MPa, which is similar to that of cortical bone, thereby eliminating the issue of stress shielding.
(4) Sintered samples with a sintering time of 90 min or less have similar corrosion resistance. There was a slight reduction in corrosion resistance (~2×) from SPS150_30 to SPS150_90 (0.214 mm/year vs. 0.394 mm/year). Nonetheless, SPS150_90 exhibited ~10× better corrosion resistance than as-cast MgZnCa (0.394 mm/year vs. 4.086 mm/year).

**Author Contributions:** Conceptualization, K.S.F. and M.G.; methodology, K.S.F. and C.B.W.; validation, S.T.; formal analysis, B.S.J.B., K.S.F., S.T. and E.S.P.; investigation, B.S.J.B., M.K.K. and E.S.P.; resources, S.T. and M.K.K.; writing—original draft, B.S.J.B.; writing—review and editing, M.G.; supervision, C.B.W. and M.G. All authors have read and agreed to the published version of the manuscript.

**Funding:** M.K.K. and E.S.P. were supported by the Creative Materials Discovery Program through the National Research Foundation of Korea (NRF) funded by the Korean Government (MSIT) (no. NRF-2019M3D1A1079215).

**Data Availability Statement:** Not applicable.

**Conflicts of Interest:** The authors declare no conflict of interest.

## References

1. González, S. Improved mechanical performance and delayed corrosion phenomena in biodegradable Mg–Zn–Ca alloys through Pd-alloying. *J. Mech. Behav. Biomed. Mater.* **2012**, *6*, 53–62. [CrossRef] [PubMed]
2. Kraus, T.; Fischerauer, S.F.; Hänzi, A.C.; Uggowitzer, P.J.; Löffler, J.F.; Weinberg, A.M. Magnesium alloys for temporary implants in osteosynthesis: In vivo studies of their degradation and interaction with bone. *Acta Biomater.* **2012**, *8*, 1230–1238. [CrossRef]
3. Lu, W.; He, M.; Yu, D.; Xie, X.; Wang, H.; Wang, S.; Yuan, C.; Chen, A. Ductile behavior and excellent corrosion resistance of Mg-Zn-Yb-Ag metallic glasses. *Mater. Des.* **2021**, *210*, 110027. [CrossRef]
4. Babaremu, K.O.; John, M.E.; Mfoh, U.; Akinlabi, E.T.; Okokpujie, I.P. Behavioral Characteristics of Magnesium as a Biomaterial for Surface Engineering Application. *J. Bio Tribo Corros.* **2021**, *7*, 142. [CrossRef]
5. Denkena, B.; Lucas, A. Biocompatible Magnesium Alloys as Absorbable Implant Materials—Adjusted Surface and Subsurface Properties by Machining Processes. *CIRP Ann.* **2007**, *56*, 113–116. [CrossRef]
6. Bin, S.J.B.; Fong, K.S.; Chua, B.W.; Gupta, M. Mg-based bulk metallic glasses: A review of recent developments. *J. Magnes. Alloys* **2021**, *10*, 899–914. [CrossRef]
7. Cai, A.H.; Xiong, X.; Yong, L.; An, W.K.; Zhou, G.J.; Yun, L.; Tie-Lin, L.; Li, X.S. Effect of consolidation parameters on mechanical properties of Cu-based bulk amorphous alloy consolidated by hot pressing. *Trans. Nonferrous Met. Soc. China* **2012**, *22*, 2032–2040. [CrossRef]
8. Lee, P.Y.; Kao, M.C.; Lin, C.K.; Huang, J.C. Mg–Y–Cu bulk metallic glass prepared by mechanical alloying and vacuum hot-pressing. *Intermetallics* **2006**, *14*, 994–999. [CrossRef]
9. Robertson, J.; Im, J.T.; Karaman, I.; Hartwig, K.T.; Anderson, I.E. Consolidation of amorphous copper based powder by equal channel angular extrusion. *J. Non Cryst. Solids* **2003**, *317*, 144–151. [CrossRef]
10. Pauly, S. Processing metallic glasses by selective laser melting. *Mater. Today* **2013**, *16*, 37–41. [CrossRef]
11. Bin, S.J.B.; Fong, K.S.; Chua, B.W.; Gupta, M. Development of Biocompatible Bulk MgZnCa Metallic Glass with Very High Corrosion Resistance in Simulated Body Fluid. *Materials* **2022**, *15*, 8989. [CrossRef] [PubMed]
12. Anselmi-Tamburini, U. Spark Plasma Sintering. In *Encyclopedia of Materials: Technical Ceramics and Glasses*; Pomeroy, M., Ed.; Elsevier: Oxford, UK, 2021; pp. 294–310. [CrossRef]
13. Cardinal, S.; Pelletier, J.M.; Qiao, J.C.; Bonnefont, G.; Xie, G. Influence of spark plasma sintering parameters on the mechanical properties of Cu50Zr45Al5 bulk metallic glass obtained using metallic glass powder. *Mater. Sci. Eng. A* **2016**, *677*, 116–124. [CrossRef]
14. Zhang, Y.N.; Rocher, G.J.; Briccoli, B.; Kevorkov, D.; Liu, X.B.; Altounian, Z.; Medraj, M. Crystallization characteristics of the Mg-rich metallic glasses in the Ca–Mg–Zn system. *J. Alloys Compd.* **2013**, *552*, 88–97. [CrossRef]
15. Jin, C.; Liu, Z.; Yu, W.; Qin, C.; Yu, H.; Wang, Z. Biodegradable Mg–Zn–Ca-Based Metallic Glasses. *Materials* **2022**, *15*, 2172. [CrossRef]
16. Shamlaye, K.F.; Löffler, J.F. Synthesis and characterization of Mg-based bulk metallic glasses in the Mg–Ag–Y–(Cu) system. *J. Alloys Compd.* **2021**, *859*, 157803. [CrossRef]
17. Yang, D.; Zhang, Y.; Song, X.; Chen, Y.; Shen, Z.; Yang, C. Effects of sintering temperature and holding time on porosity and shrinkage of glass tubes. *Ceram. Int.* **2016**, *42*, 5906–5910. [CrossRef]
18. Muhammad, W.N.A.W.; Sajuri, Z.; Mutoh, Y.; Miyashita, Y. Microstructure and mechanical properties of magnesium composites prepared by spark plasma sintering technology. *J. Alloys Compd.* **2011**, *509*, 6021–6029. [CrossRef]
19. Putra, A.G.; Manaf, A.; Anawati, A. Enhancing the Hardness of Mg-9Al-1Zn Cast Alloy by Solution Treatment. *IOP Conf. Ser. Mater. Sci. Eng.* **2019**, *515*, 012088. [CrossRef]
20. Minarik, P.; Stráský, J.; Veselý, J.; Lukáč, F.; Hadzima, B.; Kral, R. AE42 magnesium alloy prepared by spark plasma sintering. *J. Alloys Compd.* **2018**, *742*, 172–179. [CrossRef]
21. Morgan, E.F.; Unnikrisnan, G.U.; Hussein, A.I. Bone Mechanical Properties in Healthy and Diseased States. *Annu. Rev. Biomed. Eng.* **2018**, *20*, 119–143. [CrossRef]
22. Be'ery-Lipperman, M.; Gefen, A. A method of quantification of stress shielding in the proximal femur using hierarchical computational modeling. *Comput. Methods Biomech. Biomed. Engin.* **2006**, *9*, 35–44. [CrossRef]

23. Raffa, M.L.; Nguyen, V.H.; Hernigou, P.; Flouzat-Lachaniette, C.H.; Haiat, G. Stress shielding at the bone-implant interface: Influence of surface roughness and of the bone-implant contact ratio. *J. Orthop. Res.* **2021**, *39*, 1174–1183. [CrossRef] [PubMed]
24. Leslie, N.; Mauzeroll, J. Spatially resolved electrochemical measurements. In *Reference Module in Chemistry, Molecular Sciences and Chemical Engineering*; Elsevier: Amsterdam, The Netherlands, 2023. [CrossRef]
25. Chen, J.; Zhu, X.; Etim, I.P.; Siddiqui, M.A.; Su, X. Comparative study of the effects of MAO coating and Ca-P coating on the biodegradation and biocompatibility of Mg 69 Zn 27 Ca 4 metal glass. *Mater. Technol.* **2020**, *37*, 21–27. [CrossRef]
26. Zhang, Y.; Yan, C.; Wang, F.; Li, W. Electrochemical behavior of anodized Mg alloy AZ91D in chloride containing aqueous solution. *Corros. Sci.* **2005**, *47*, 2816–2831. [CrossRef]
27. Gu, X.; Zheng, Y.; Zhong, S.; Xi, T.; Wang, J.; Wang, W. Corrosion of, and cellular responses to Mg–Zn–Ca bulk metallic glasses. *Biomaterials* **2010**, *31*, 1093–1103. [CrossRef]
28. Ford, D.C.; Hicks, D.; Oses, C.; Toher, C.; Curtarolo, S. Metallic glasses for biodegradable implants. *Acta Mater.* **2019**, *176*, 297–305. [CrossRef]
29. Noviana, D.; Paramitha, D.; Ulum, M.F.; Hermawan, H. The effect of hydrogen gas evolution of magnesium implant on the postimplantation mortality of rats. *J. Orthop. Transl.* **2016**, *5*, 9–15. [CrossRef] [PubMed]
30. Rybalka, K.V.; Beketaeva, L.A.; Davydov, A.D. Determination of corrosion current density by the rate of cathodic depolarizer consumption. *Russ. J. Electrochem.* **2016**, *52*, 268–272. [CrossRef]
31. Balani, K.; Verma, V.; Agarwal, A.; Narayan, R. Corrosion Behavior of Metals. In *Biosurfaces*; John Wiley & Sons, Ltd.: New York, NY, USA, 2014; pp. 345–352. [CrossRef]
32. Schmidt, H.; Gruber, W.; Gutberlet, T.; Ay, M.; Stahn, J.; Geckle, U.; Bruns, M. Structural relaxation and self-diffusion in covalent amorphous solids: Silicon nitride as a model system. *J. Appl. Phys.* **2007**, *102*, 043516. [CrossRef]
33. Lee, D.; Vlassak, J.J. Diffusion kinetics in binary CuZr and NiZr alloys in the super-cooled liquid and glass states studied by nanocalorimetry. *Scr. Mater.* **2019**, *165*, 73–77. [CrossRef]
34. Syutkin, V.M.; Grebenkin, S. Diffusion in bulk metallic glasses. *Appl. Phys. Lett.* **2020**, *117*, 134104. [CrossRef]
35. Lazarus, D. Diffusion in Crystalline and Amorphous Solids. *MRS Online Proc. Libr. (OPL)* **1985**, *57*, 297. [CrossRef]
36. Suárez, M.; Fernández-González, D.; Díaz, L.A.; Diologent, F.; Verdeja, L.F.; Fernández, A. Consolidation and mechanical properties of ZrCu39.85Y2.37Al1.8 bulk metallic glass obtained from gas-atomized powders by spark plasma sintering. *Intermetallics* **2021**, *139*, 107366. [CrossRef]
37. Paul, T.; Singh, A.; Littrell, K.C.; Ilavsky, J.; Harimkar, S.P. Crystallization Mechanism in Spark Plasma Sintered Bulk Metallic Glass Analyzed using Small Angle Neutron Scattering. *Sci. Rep.* **2020**, *10*, 2033. [CrossRef]
38. Zheng, B.; Ashford, D.; Zhou, Y.; Mathaudhu, S.N.; Delplanque, J.P.; Lavernia, E.J. Influence of mechanically milled powder and high pressure on spark plasma sintering of Mg–Cu–Gd metallic glasses. *Acta Mater.* **2013**, *61*, 4414–4428. [CrossRef]
39. Perrière, L.; Champion, Y.; Bernard, F. Spark Plasma Sintering of Metallic Glasses. In *Spark Plasma Sintering of Materials: Advances in Processing and Applications*; Cavaliere, P., Ed.; Springer International Publishing: Cham, Switzerland, 2019; pp. 291–335. [CrossRef]
40. Tyagi, A.K.; Macht, M.P.; Naundorf, V. Diffusion coefficients of 63Ni in Fe40Ni40B20 metallic glass. *Acta Metall. Mater.* **1991**, *39*, 609–617. [CrossRef]
41. Perrière, L.; Thaï, M.T.; Tusseau-Nenez, S.; Ochin, P.; Blétry, M.; Champion, Y. Spark plasma sintering for metallic glasses processing. *Rev. Métallurgie* **2012**, *109*, 5–10. [CrossRef]
42. Ajenifuja, E.; Odetola, P.; Popoola, A.P.; Popoola, O. Spark plasma sintering and structural analysis of nickel-titanium/coconut shell powder metal matrix composites. *Int. J. Adv. Manuf. Technol.* **2020**, *108*, 3465–3473. [CrossRef]
43. Olson, G.L.; Roth, J.A. Kinetics of solid phase crystallization in amorphous silicon. *Mater. Sci. Rep.* **1988**, *3*, 1–77. [CrossRef]
44. Yavari, A.R.; Le Moulec, A.; Inoue, A.; Nishiyama, N.; Lupu, N.; Matsubara, E.; José Botta, W.; Vaughan, G.; Di Michiel, M.; Kvick, Å. Excess free volume in metallic glasses measured by X-ray diffraction. *Acta Mater.* **2005**, *53*, 1611–1619. [CrossRef]


**Disclaimer/Publisher's Note:** The statements, opinions and data contained in all publications are solely those of the individual author(s) and contributor(s) and not of MDPI and/or the editor(s). MDPI and/or the editor(s) disclaim responsibility for any injury to people or property resulting from any ideas, methods, instructions or products referred to in the content.